

Crystal structure of the plasma membrane proton pump

Bjørn P. Pedersen^{1,2*}, Morten J. Buch-Pedersen^{1,2,3*}, J. Preben Morth^{1,2}, Michael G. Palmgren^{1,3} & Poul Nissen^{1,2}

A prerequisite for life is the ability to maintain electrochemical imbalances across biomembranes. In all eukaryotes the plasma membrane potential and secondary transport systems are energized by the activity of P-type ATPase membrane proteins: H⁺-ATPase (the proton pump) in plants and fungi^{1–3}, and Na⁺,K⁺-ATPase (the sodium–potassium pump) in animals⁴. The name P-type derives from the fact that these proteins exploit a phosphorylated reaction cycle intermediate of ATP hydrolysis⁵. The plasma membrane proton pumps belong to the type III P-type ATPase subfamily, whereas Na⁺,K⁺-ATPase and Ca²⁺-ATPase are type II⁶. Electron microscopy has revealed the overall shape of proton pumps⁷, however, an atomic structure has been lacking. Here we present the first structure of a P-type proton pump determined by X-ray crystallography. Ten transmembrane helices and three cytoplasmic domains define the functional unit of ATP-coupled proton transport across the plasma membrane, and the structure is locked in a functional state not previously observed in P-type ATPases. The transmembrane domain reveals a large cavity, which is likely to be filled with water, located near the middle of the membrane plane where it is lined by conserved hydrophilic and charged residues. Proton transport against a high membrane potential is readily explained by this structural arrangement.

The *Arabidopsis thaliana* auto-inhibited H⁺-ATPase 2 (AHA2) is a well-characterized member of the plasma membrane proton pump family⁸. As shown in Fig. 1, we have determined the structure of an active form of AHA2, devoid of a flexible, carboxy-terminal regulatory domain (R domain)^{3,9} and in complex with adenosine 5'-(β,γ-methylene)-triphosphate (AMPPCP, a non-hydrolysable ATP analogue). Despite anisotropy of the data, we successfully traced the structure and refined a model encompassing residues 12 to 844 and the bound nucleotide on the basis of experimental electron-density maps calculated at 3.6 Å resolution (Fig. 2a, b, Supplementary Table 1 and Supplementary Fig. 1).

The structure of AHA2 consists of four clearly defined domains: a transmembrane domain with ten helices, M1 through M10, and three cytosolic domains, named after their counterparts in the Ca²⁺-ATPase¹⁰ as N (nucleotide binding; residues 338–488), P (phosphorylation; residues 308–337 and 489–625) and A (actuator; residues 12–57 and 129–233). AHA2 and the rabbit SERCA1a Ca²⁺-ATPase share low sequence homology (20% identity; Supplementary Fig. 2), but a structural comparison shows the overall fold to be remarkably similar, supporting the assumption that the overall structure of P-type ATPases is conserved among different subfamilies (Fig. 2c, d). However, the N domain of AHA2 is smaller than the N domains found in the type II subfamily. It has the same fold as the N domain of the *Archaeoglobus fulgidus* copper pump¹¹, although the loops

connecting strand 3 to strand 4 and strand 5 to strand 6 are longer and resemble the loops found in Ca²⁺-ATPase¹⁰ and Na⁺,K⁺-ATPase¹². AMPPCP is bound with the adenosine part at the N domain and the triphosphate group protruding towards the P domain (Figs 1 and 2a). The N domain is inserted into the P domain through a hinge (including the conserved sequence motif DPPR) and with bound nucleotide it can move towards the P domain

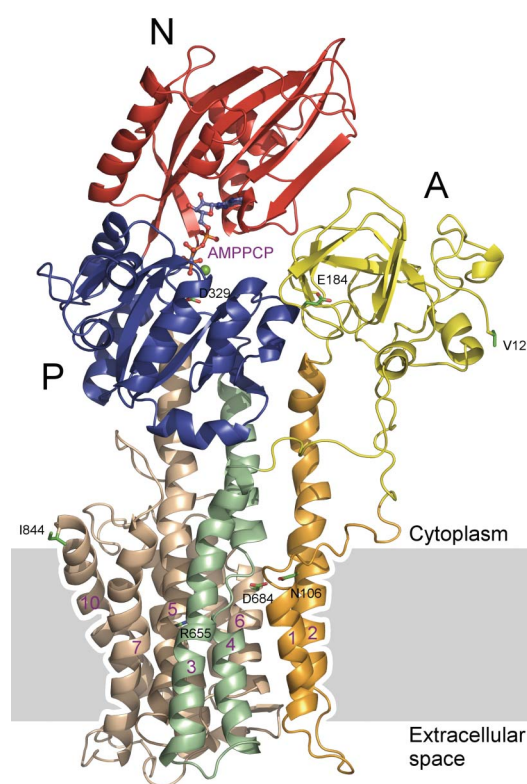


Figure 1 | Overall structure of the plasma membrane H⁺-ATPase. The structure represents an active form of the proton pump, without its auto-inhibitory C terminus, in complex with Mg-AMPPCP. Ten transmembrane helices, orange, green and brown, as indicated; nucleotide-binding domain (N), red; the phosphorylation domain (P), blue; and the actuator domain (A), yellow. Mg-AMPPCP is found at the interface between the N and P domains and is shown as a ball-and-stick representation. Key residues mentioned in the text are shown as sticks. The grey box depicts the approximate location of the plasma membrane.

¹Centre for Membrane Pumps in Cells and Disease—PUMPKIN, Danish National Research Foundation, ²Department of Molecular Biology, University of Aarhus, Gustav Wieds Vej 10C, DK-8000 Aarhus, Denmark. ³Plant Physiology and Anatomy Laboratory, Department of Plant Biology, University of Copenhagen, Thorvaldsensvej 40, DK-1871 Frederiksberg, Denmark.

*These authors contributed equally to this work.

to assemble the catalytic site, at which Asp 329 will become phosphorylated once every pumping cycle. The A domain, which stimulates dephosphorylation of Asp 329, is situated on top of M2, which protrudes as a pole out of the membrane, and it is further connected to the M1 and M3 transmembrane segments by extended loops. Glu 184 in the conserved motif TGES, which is involved in the A domain phosphatase functionality, is situated ~ 28 Å from Asp 329. This affirms that a large rotation of the A domain towards the P domain is required for dephosphorylation to occur, linking events at the phosphorylation site to conformational changes in the membrane. In the transmembrane domain, the M1 helix shows a prominent 90° kink (Fig. 2b) imposed by a proline residue, Pro 68, that is conserved in type III P-type ATPases⁶. A similar kink is seen in the Ca^{2+} -ATPase¹³ and Na^+, K^+ -ATPase¹², despite distinct motifs in the M1 primary structure for each type. M4 is unwound in the middle of the transmembrane segment, and M7 and M10 are tilted approximately 25° and 45° , respectively, relative to the plane of the membrane.

The overall arrangement of domains and transmembrane helices of AHA2 is similar, but not identical, to the occluded E1 form of Ca^{2+} -ATPase trapped in the transition state of phosphoryl transfer^{14,15} (Fig. 2d). The A domain is moved away from the P domain,

allowing the N domain to approach as required for phosphorylation to occur, but closure of the active site at the interface between the N and P domains has not completed. Further comparison to the AMPPCP-bound E2 form of Ca^{2+} -ATPase¹⁶ (Fig. 2d) indicates that our AHA2 structure indeed represents a new E1 intermediate, which is compact, yet not completely occluded.

Auto-inhibition by C-terminal regulatory R domains is characteristic of type III P-type H^+ -ATPases. We have obtained crystals and collected a 5.5 Å resolution data set of full-length AHA2 in a detergent-activated form. We observe additional electron density for approximately 13 residues (modelled as a helix) of the R domain, extending from the M10 helix towards a large solvent channel in the crystal (Supplementary Fig. 3). However, we do not observe density for the bulk of the R domain (residue 858 to 948), indicating that it has no defined structure in the active form of the protein. If we plot residues that, when mutated, inhibit R domain interaction (shown by mutagenesis of plant and fungal P-type proton pumps^{2,17,18}), a pattern emerges in which the R domain may attain inhibition by winding around the body of the pump to interact with the A domain and the top of the M1 and M2 segments. In this position, the R domain potentially blocks entry of protons to the transmembrane binding site and restricts A domain rotations that are essential for functional transitions in the pumping cycle. This is much like the fixation by thapsigargin of the transmembrane domain in Ca^{2+} -ATPase¹⁴, and possibly similar to the effect of regulatory peptides like sarcolipin and phospholamban¹⁹.

Asp 684, conserved in all plasma membrane H^+ -ATPases, is the only acidic residue buried in the transmembrane domain of AHA2 (Fig. 3a). Mutational studies have shown this residue to be essential for proton transport and E1–E2 transitions, and thus the most likely candidate for the proton-binding site of P-type H^+ -ATPases^{9,20}. Asp 684 corresponds to the essential Ca^{2+} -coordinating residue Asp 800 in the Ca^{2+} -ATPase and it is situated in M6, next to a large cavity in the membrane (Fig. 2c, see below). Asp 684 is juxtaposed to the completely conserved Asn 106 of M2 (Fig. 3b, c), which is compatible with hydrogen bonding between the two. This feature suggests an elegant coupling mechanism of H^+ -ATPase between formation of the phosphorylation site in the cytoplasmic domains and occlusion of the proton-binding site with the protonated Asp 684 and Asn 106 pair buried between the M2, M4 and M6 segments. This will also readily explain the proton specificity of H^+ -ATPase; the specificity arises at the protonated Asp 684–Asn 106 pair, which serves as the ‘gate keeper’ along the transport pathway.

Owing to a conserved Pro 286 residue, M4 is unwound, which leads to exposure of backbone carbonyl and amide groups from residues 282–286 to a large cavity in the middle of the membrane (Fig. 3). The conserved residues Tyr 645, Tyr 648, Thr 653, Arg 655 (all in M5) and Asn 683 (in M6) expose their charged or polar side chains to this cavity. The corresponding residues in M5 of the yeast PMA1 H^+ -ATPase (Tyr 691, Tyr 694, Ser 699 and His 701) have been shown to be essential for proton pumping²¹. The cavity is defined by M4, M5 and M6 (Fig. 3), and in dimensions it is substantially bigger than the Ca^{2+} -binding sites I and II of the Ca^{2+} -ATPase¹⁰. The enlargement is mainly due to M6, which is bulged at Asp 684 (Fig. 2c, and Supplementary Fig. 4). The cavity is large enough (~ 380 Å³) to accommodate about 12 water molecules. Proton access from the cytoplasm to the proton-binding site seems nearly closed in our structure, but could occur through an entrance pathway located between M1, M2 and M4 (Fig. 3a). Several conserved H^+ -ATPase residues are positioned in this area of the pump, for example, Asn 106, Glu 113, Glu 114 (all in M2), and they could be involved in proton transfer to Asp 684 at the edge of the cavity.

Arg 655 of M5 is situated in the middle of the membrane domain, at the cavity opposite to the Asp 684 residue (Fig. 3). Arg 655 is important, but not indispensable, for proton transport²⁰. The interaction of Arg 655 with the, presumably water-filled, cavity is well defined, even though the exact side-chain structure is not at the given

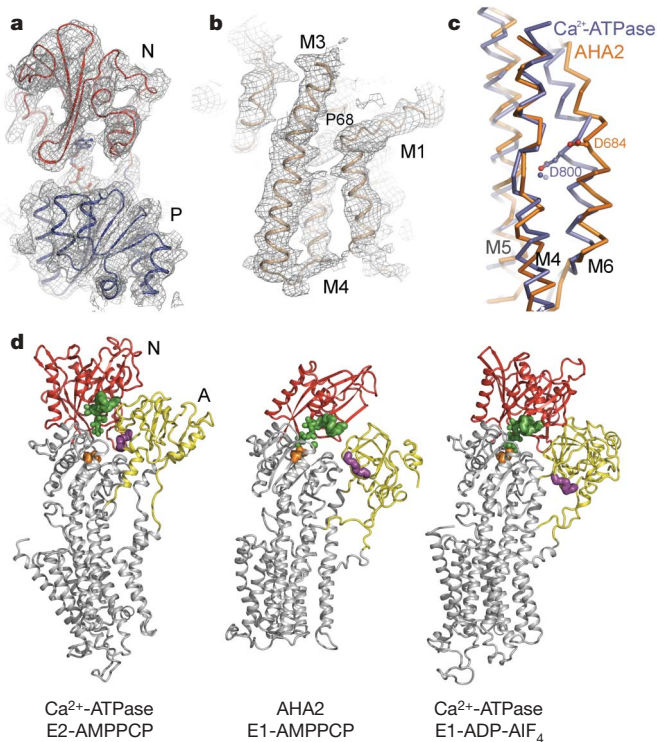


Figure 2 | Structural conservation of P-type ATPase architecture. **a**, View of the N (red) and P (blue) domains of the H^+ -ATPase with bound Mg-AMPPCP together with the experimental electron-density map contoured at 1σ . The adenosine of the nucleotide is bound at the N domain, whereas the triphosphate group and the magnesium ion extend towards the P domain. **b**, View of the transmembrane region with the experimental electron-density map contoured at 1σ . M1 exhibits a $\sim 90^\circ$ kink perpendicular to the membrane face facilitated by Pro 68. **c**, AHA2 (orange) is aligned to the Ca^{2+} -ATPase (blue, PDB code 1T5T) on transmembrane segments M4 and M5. The bulge at Asp 684 is clearly visible. **d**, Structural comparison between AHA2 and Ca^{2+} -ATPase indicates that the H^+ -ATPase structure represents a novel E1 intermediate. Middle panel, AHA2 H^+ -ATPase with bound Mg-AMPPCP (this study); left panel, an E2 form of the Ca^{2+} -ATPase without bound calcium (PDB code 2C8K); right panel, a Ca^{2+} -occluded E1 form of the Ca^{2+} -ATPase^{15,16} in the transition state of phosphoryl transfer (PDB code 1T5T). The structures are aligned by their P domains. N domain, red; bound nucleotide, green; A-domain, yellow; TGES motif required for dephosphorylation, magenta; phosphorylation site, orange.

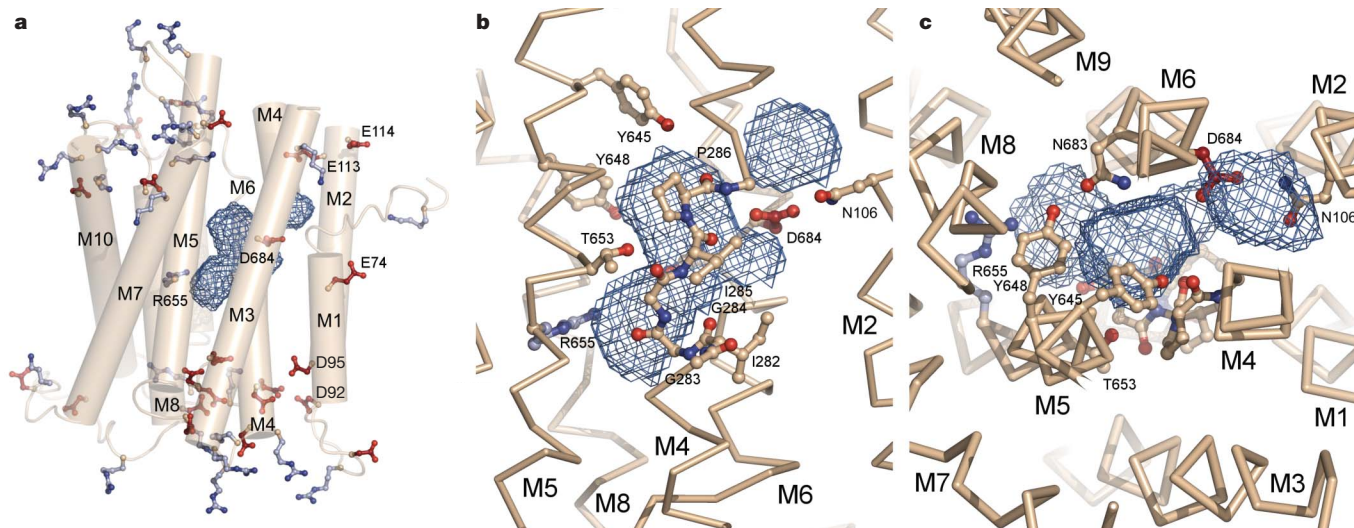


Figure 3 | The intramembranous buried cavity and proton binding site of the plasma membrane H^+ -ATPase. **a**, Distribution of charged residues (Arg/Lys, blue; Asp/Glu, red) in the transmembrane region of the pump shown together with the identified intramembranous cavity (blue mesh). Among the charged residues in this region, Arg 655 and Asp 684 are the only two charged residues found in the transmembrane part (except Glu 74 of M1, which points towards the cytosolic interface). **b**, Side view and **c**, top

view of the cavity and the residues lining it. Polar and charged residues from M5 and M6 together with exposed backbone carbonyls and amide groups from M4 define the boundaries of the cavity. A small extension ($\sim 80 \text{ \AA}^3$) of the cavity, placed over Asp 684 and Asn 106, is located along the expected proton entrance pathway and is likely to close as the phosphorylation site is fully assembled.

resolution. Owing to the packing of nearby membrane residues, Arg 655 is confined to side-chain rotamer configurations pointing upwards towards Asp 684 and in direct contact with the cavity. The cavity may aid in delocalization of the buried positive charge on Arg 655 as the pump goes through phosphorylation and it may form the upper part of the proton exit pathway during subsequent proton release. The electrostatic field of Arg 655 is likely to influence Asp 684. A spatial arrangement of an arginine residue placed near an essential proton donor/acceptor is well characterized in unrelated proton pumps like bacteriorhodopsin^{22,23} and F-/V-type ATPases^{24,25} as a means of stimulating proton release, and we find it likely that a similar role is achieved here. Arg 655 must be expected to impose an effect on Asp 684 in the E2P state, in which the proton exit pathway opens to the extracellular environment. Also, the presence of similarly conserved positive-negative amino acid pairs of M5/M6 in H^+ , K^+ -ATPases (for example, Lys 800 and Asp 833 of the human ATPase ATP12A) at equivalent positions hints at a conserved mechanism of proton transport in proton-exporting P-type ATPases. Proton release from the pump might be aided by conserved acidic residues (for example, Asp 92 and Asp 95) found at the extracellular side (Fig. 3a).

Arg 655 may serve other important roles. The corresponding residue in Ca^{2+} -ATPase is Glu 771, which becomes exposed at the bottom of the Ca^{2+} exit pathway in the E2P form²⁶. Likewise, Arg 655 may become exposed in the proton exit pathway of AHA2. In this position, it could serve as a positive plug that prevents proton reflux to the transmembrane binding site (Fig. 4). A positive charge along the transport pathway may then explain how proton pumps are able to generate high membrane potentials. In plants, membrane potentials may exceed -200 mV (negative on the inside; ref. 27), whereas the proton pumps from fungi generate the highest known membrane potentials (up to -300 mV ; ref. 28). In fungal H^+ -ATPases, Arg 655 of AHA2 is replaced by a histidine (His 701 in yeast PMA1), whereas another arginine is found at the 649 position of the M5 helix, also facing the water-filled cavity. This arrangement of an arginine and a histidine positioned in tandem at the upper part of the proton exit pathway is indeed compatible with the even-higher resistance to membrane potential that is attained in fungal proton pumps. No counter transport during the E2 to E1 transition has been described for proton pumps; this is in contrast to other subfamilies of P-type

ATPases. Arg 655 may act as a built-in counter-ion during dephosphorylation and E2 to E1 transition, neutralizing the deprotonated negatively charged Asp 684. The presence of Arg 655 as a constitutive counter-ion makes the transition from E2-P to E2 extremely favourable and minimizes exposure of Asp 684 to the extracellular side. This is consistent with the fact that proton pumps cannot be directly phosphorylated by inorganic phosphate, contrary to other P-type

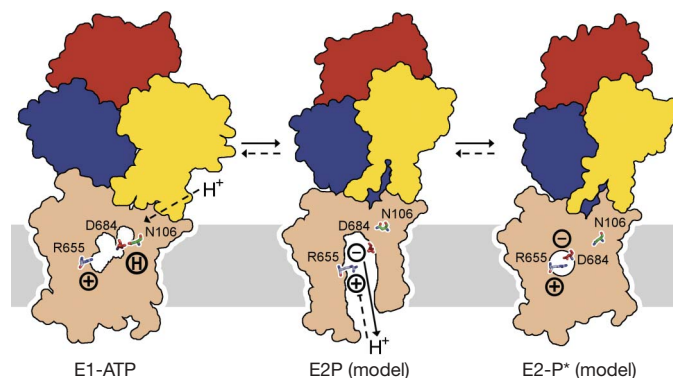


Figure 4 | Mechanism of proton transport by plasma membrane H^+ -ATPase. E2-model forms of the H^+ -ATPase were made by structural alignment of our E1-AMPPCP structure with the E2P structure of the Ca^{2+} -ATPase²⁶ and the E2-P* structure (E2 occluded state of the pump) of the Ca^{2+} -ATPase (PDB code 1XP5). Asp 684 is the central proton donor/acceptor of the pump, and together with Arg 655 it lines a centrally located water-filled cavity. In the E1 conformation, hydrogen bonding between Asp 684 and Asn 106 gives preference to the protonated form of Asp 684 (E1-ATP structure). Conformational movements in the membrane region, coupled to E1-E2 transitions, result in opening of the cavity towards the proton exit pathway (E2P model) and interrupt hydrogen bonding between Asn 106 and Asp 684; this results in proton release from Asp 684, now exposed to the extracellular environment. Placement of Arg 655 towards Asp 684 at the exit channel also stimulates proton release from Asp 684, and provides a positively charged plug in this area of the molecule that prevents extracellular protons from re-protonating Asp 684. At the same time Arg 655 functions as a built-in counter-ion that neutralizes the negative charge on Asp 684 and promotes swift formation of the occluded E2-P* transition state (E2P* model), dephosphorylation and transition to the E2 form.

ATPase subfamilies²⁹. The price of being able to sustain a high membrane potential may thus be the loss of counter transport. Indeed the apparent stoichiometry of P-type H⁺-ATPase transport is one proton per ATP hydrolysed³⁰.

The structure described here contributes to further understanding of the structural/functional relationships found in plant and fungal P-type H⁺-ATPases and furthermore provides a framework for new studies of members of this subfamily. Our observation of an Asp–Asn pair and an arginine residue lining a water-filled cavity in the membrane represent key elements of proton transport by proton P-type ATPases and a novel use of the P-type ATPase architecture for active transport.

METHODS SUMMARY

Expression and purification was based on a *Saccharomyces cerevisiae* expression system. Solubilization and purification were performed with dodecyl-maltoside (DDM) as the detergent and the purified protein was dialysed against a buffer containing octaethylene glycol monododecyl ether (C₁₂E₈) and 5-cyclohexyl-1-pentyl-β-D-maltoside (CYMAL-5) detergents. Crystals were obtained using polyethylene glycol 400 as the precipitant. Crystals were cryoprotected by a controlled dehydration procedure by vapour diffusion, which also improved diffraction properties. Crystallographic data were collected at the beam line X06SA of the Swiss Light Source (SLS). Phases were determined using derivative crystals with HoCl₃, K₂PtCl₆ and Ta₆Br₁₂, respectively. Heavy-atom-derived phases were refined and extended to the maximum resolution of the native data by density modification, exploiting two-fold rotational non-crystallographic symmetry, a solvent content of 75% and several data sets showing a low level of isomorphism for inter-crystal averaging. The experimental electron density was of high quality, showing continuous backbone density but lacking detail owing to anisotropy and low resolution of the data (Fig. 2, and Supplementary Fig. 4). Final refinement using data extending to 3.6 Å resolution produced a model with a crystallographic R-factor of 35.0% and a free R-factor of 36.6%.

Full Methods and any associated references are available in the online version of the paper at www.nature.com/nature.

Received 20 August; accepted 26 October 2007.

- Serrano, R., Kielland-Brandt, M. C. & Fink, G. R. Yeast plasma membrane ATPase is essential for growth and has homology with (Na⁺ + K⁺), K⁺- and Ca²⁺-ATPases. *Nature* **319**, 689–693 (1986).
- Morsomme, P., Slayman, C. W. & Goffeau, A. Mutagenic study of the structure, function and biogenesis of the yeast plasma membrane H⁺-ATPase. *Biochim. Biophys. Acta* **1469**, 133–157 (2000).
- Palmgren, M. G. Plant plasma membrane H⁺-ATPases: Powerhouses for nutrient uptake. *Annu. Rev. Plant Physiol. Plant Mol. Biol.* **52**, 817–845 (2001).
- Skou, J. C. & Esmann, M. The Na,K-ATPase. *J. Bioenerg. Biomembr.* **24**, 249–261 (1992).
- Pedersen, P. & Carafoli, E. Ion motive ATPases. 1. Ubiquity, properties, and significance to cell function. *Trends Biochem. Sci.* **12**, 146–150 (1987).
- Axelsen, K. B. & Palmgren, M. G. Evolution of substrate specificities in the P-type ATPase superfamily. *J. Mol. Evol.* **46**, 84–101 (1998).
- Auer, M., Scarborough, G. A. & Kuhlbrandt, W. Three-dimensional map of the plasma membrane H⁺-ATPase in the open conformation. *Nature* **392**, 840–843 (1998).
- Harper, J. F., Manney, L., DeWitt, N. D., Yoo, M. H. & Sussman, M. R. The *Arabidopsis thaliana* plasma membrane H⁺-ATPase multigene family. Genomic sequence and expression of a third isoform. *J. Biol. Chem.* **265**, 13601–13608 (1990).
- Buch-Pedersen, M. J., Venema, K., Serrano, R. & Palmgren, M. G. Abolishment of proton pumping and accumulation in the E1P conformational state of a plant plasma membrane H⁺-ATPase by substitution of a conserved aspartyl residue in transmembrane segment 6. *J. Biol. Chem.* **275**, 39167–39173 (2000).
- Toyoshima, C., Nakasako, M., Nomura, H. & Ogawa, H. Crystal structure of the calcium pump of sarcoplasmic reticulum at 2.6 Å resolution. *Nature* **405**, 647–655 (2000).
- Sazinsky, M. H., Mandal, A. K., Arguello, J. M. & Rosenzweig, A. C. Structure of the ATP binding domain from the *Archaeoglobus fulgidus* Cu⁺-ATPase. *J. Biol. Chem.* **281**, 11161–11166 (2006).

- Morth, J. P. *et al.* Crystal structure of the sodium–potassium pump. *Nature* doi:10.1038/nature06419 (this issue).
- Toyoshima, C. & Nomura, H. Structural changes in the calcium pump accompanying the dissociation of calcium. *Nature* **418**, 605–611 (2002).
- Sorensen, T. L., Møller, J. V. & Nissen, P. Phosphoryl transfer and calcium ion occlusion in the calcium pump. *Science* **304**, 1672–1675 (2004).
- Toyoshima, C. & Mizutani, T. Crystal structure of the calcium pump with a bound ATP analogue. *Nature* **430**, 529–535 (2004).
- Jensen, A. M., Sørensen, T. L., Olesen, C., Møller, J. V. & Nissen, P. Modulatory and catalytic modes of ATP binding by the calcium pump. *EMBO J.* **25**, 2305–2314 (2006).
- Eraso, P. & Portillo, F. Molecular mechanism of regulation of yeast plasma membrane H⁺-ATPase by glucose. Interaction between domains and identification of new regulatory sites. *J. Biol. Chem.* **269**, 10393–10399 (1994).
- Morsomme, P., Dambly, S., Maudoux, O. & Boutry, M. Single point mutations distributed in 10 soluble and membrane regions of the *Nicotiana plumbaginifolia* plasma membrane PMA2 H⁺-ATPase activate the enzyme and modify the structure of the C-terminal region. *J. Biol. Chem.* **273**, 34837–34842 (1998).
- MacLennan, D. H., Abu-Abed, M. & Kang, C. Structure–function relationships in Ca²⁺ cycling proteins. *J. Mol. Cell. Cardiol.* **34**, 897–918 (2002).
- Buch-Pedersen, M. J. & Palmgren, M. G. Conserved Asp684 in transmembrane segment M6 of the plant plasma membrane P-type proton pump AHA2 is a molecular determinant of proton translocation. *J. Biol. Chem.* **278**, 17845–17851 (2003).
- Dutra, M. B., Ambesi, A. & Slayman, C. W. Structure–function relationships in membrane segment 5 of the yeast Pma1 H⁺-ATPase. *J. Biol. Chem.* **273**, 17411–17417 (1998).
- Pebay-Peyroula, E., Rummel, G., Rosenbusch, J. P. & Landau, E. M. X-ray structure of bacteriorhodopsin at 2.5 angstroms from microcrystals grown in lipidic cubic phases. *Science* **277**, 1676–1681 (1997).
- Luecke, H., Richter, H. T. & Lanyi, J. K. Proton transfer pathways in bacteriorhodopsin at 2.3 angstrom resolution. *Science* **280**, 1934–1937 (1998).
- Hutcheon, M. L., Duncan, T. M., Ngai, H. & Cross, R. L. Energy-driven subunit rotation at the interface between subunit a and the c oligomer in the F₀ sector of *Escherichia coli* ATP synthase. *Proc. Natl. Acad. Sci. USA* **98**, 8519–8524 (2001).
- Fillingame, R. H. & Dmitriev, O. Y. Structural model of the transmembrane F₀ rotary sector of H⁺-transporting ATP synthase derived by solution NMR and intersubunit cross-linking *in situ*. *Biochim. Biophys. Acta* **1565**, 232–245 (2002).
- Olesen, C. *et al.* The structural basis of calcium transport by the calcium pump. *Nature* doi:10.1038/nature06418 (this issue).
- Hirsch, R. E., Lewis, B. D., Spalding, E. P. & Sussman, M. R. A role for the AKT1 potassium channel in plant nutrition. *Science* **280**, 918–921 (1998).
- Blatt, M. R., Rodriguez-Navarro, A. & Slayman, C. L. Potassium–proton symport in *Neurospora*: Kinetic control by pH and membrane potential. *J. Membr. Biol.* **98**, 169–189 (1987).
- Amory, A., Goffeau, A., McIntosh, D. B. & Boyer, P. D. Exchange of oxygen between phosphate and water catalyzed by the plasma membrane ATPase from the yeast *Schizosaccharomyces pombe*. *J. Biol. Chem.* **257**, 12509–12516 (1982).
- Briskin, D. P. & Reynolds-Niesman, I. Determination of H⁺/ATP stoichiometry for the plasma membrane H⁺-ATPase from red beet (*Beta vulgaris* L.) storage tissue. *Plant Physiol.* **95**, 242–250 (1991).

Supplementary Information is linked to the online version of the paper at www.nature.com/nature.

Acknowledgements We thank T. L.-M. Sørensen for contributions to initial project design and E. Pohl, C. Schulze-Briese and T. Tomizaki for assistance with synchrotron data collection. We are grateful to A. M. Nielsen for technical assistance and L. Yatime for help with data collection. B.P.P. is supported by a PhD fellowship from the Graduate School of Science at the University of Aarhus, M.J.B.-P. by a post-doctoral fellowship from the Carlsberg Foundation, J.P.M. by a post-doctoral fellowship from the DANSYNC programme of the Danish Research Council, and P.N. by a Hallas-Møller stipend from the Novo Nordisk Foundation.

Author Contributions B.P.P. performed crystallization experiments, collected and processed the data, and determined, refined and analysed the structure. M.J.B.-P. performed expression and protein purification, and later performed crystallization experiments and analysed the structure. J.P.M. assisted in data collection and processing. M.G.P. and P.N. contributed with equal resources, supervised the project and analysed the structure.

Author Information Coordinates and structure factors have been deposited in the Protein Data Bank with the accession number 3B8C. Reprints and permissions information is available at www.nature.com/reprints. Correspondence and requests for materials should be addressed to P.N. (pn@mb.au.dk) and M.G.P. (palmgren@life.ku.dk).

METHODS

Sample preparation. A *Saccharomyces cerevisiae* expression construct contained nucleotides coding for a C-terminal truncated version of the AHA2 protein lacking the last 73 residues⁹. The construct includes a MRGSH6 C-terminal tag. The construct encoding wild-type protein contained nucleotides coding for amino acid 1 to 948, including the same tag. Transformed yeast were grown and harvested essentially as described⁹. Yeast were resuspended in 50 mM Mes-KOH, pH 6.5, 26% (v/v) glycerol, 50 mM KCl, 10 mM EDTA, 1 mM dithiothreitol (DTT), 1.2 mM ATP, 0.3 mM phenylmethylsulfonyl fluoride (PMSF) and 3 $\mu\text{g ml}^{-1}$ pepstatin A before being broken mechanically using glass beads at 4 °C. After cell breakage, the homogenate was centrifuged for 5 min at 1,400g. Centrifugation of the supernatant (15 min, 12,000g) was followed by sedimentation of microsomal membranes by ultracentrifugation at 50,000 r.p.m. for 1 h (Beckman 70Ti rotor). An additional ultracentrifugation step at 50,000 r.p.m. for 1 h (Beckman 70Ti rotor) after resuspension of the pellet in GMEKD (50 mM Mes, pH 6.5), 20% (v/v) glycerol, 1 mM EDTA, 1 mM DTT, 50 mM KCl) supplemented with 0.2 mM PMSF and 2 $\mu\text{g ml}^{-1}$ pepstatin A, allowed harvesting and homogenization of the total membrane fraction in the same buffer. Membrane proteins were solubilized at 10 mg ml⁻¹ using DDM as a detergent to protein ratio of 3:1 (w/w) in 50 mM Mes-KOH, pH 6.5, 20% (v/v) glycerol, 50 mM KCl, 0.7 mM DTT and 0.7 mM EDTA. Solubilization was performed with gentle stirring for 30 min, after which unsolubilized material was removed by ultracentrifugation for 1 h at 30,000 r.p.m. (Beckman 70Ti rotor). Solubilized protein was diluted with 1 volume of 50 mM Mes, pH 6.5, 20% (v/v) glycerol, 500 mM KCl, 20 mM imidazole, 0.15% (w/v) DDM including 6–8 ml Ni-NTA resin pre-equilibrated in the same buffer. PMSF and pepstatin A were added to final concentrations of 0.2 mM and 2 $\mu\text{g ml}^{-1}$, respectively, and, following batch binding for 16 h, the resin was washed with 30 volumes of wash buffer (50 mM Mes-KOH, pH 6.5, 20% (v/v) glycerol, 5 mM imidazole, 0.15% (w/v) DDM, 0.5 mM EDTA, 0.5 mM DTT, 0.2 mM PMSF, 2 $\mu\text{g ml}^{-1}$ pepstatin) supplemented with 500 mM KCl, with 20 volumes of wash buffer with 250 mM KCl, and 20 volumes of wash buffer with 50 mM KCl before bound protein was eluted with 50 mM Mes-KOH, pH 6.5, 20% (v/v) glycerol, 200 mM imidazole, 0.04% (w/v) DDM, 50 mM KCl 0.5 mM EDTA, 0.5 mM DTT, 0.2 mM PMSF and 2 $\mu\text{g ml}^{-1}$ pepstatin A. Eluted protein were dialysed against GMEKD and concentrated to 20–30 mg ml⁻¹ on spin columns. Before crystallization experiments, protein was dialysed overnight against 50 mM KCl, 50 mM Mes pH 6.5, 10% sucrose (w/v), 1 mM DTT, 0.09 mM (critical micelle concentration) octaethyleneglycol mono-*n*-dodecylether (C₁₂E₈) and 2.4 mM (critical micelle concentration) 5-cyclohexyl-1-pentyl- β -D-maltoside (Cymal-5). After dialysis, 5 mM AMPPCP and 15 mM MgCl₂ were added and a final ultracentrifugation spin (70,000 r.p.m., 15 min) was applied before the crystallization setup.

Crystal Growth. Crystals were grown at 4 °C using the vapour diffusion method in 4 μl hanging drops with a reservoir containing 29–32% (w/v) PEG 400, 100 mM KCl, 100 mM Mes, pH 6.0, and 5% sucrose. Crystals, with a final size of around 100 \times 100 \times 200 μm^3 obtained after typically two weeks crystal growth, were dehydrated by step-wise increase of the PEG 400 concentration in the reservoir solution to 40%. Dehydrated crystals were mounted in nylon loops and flashcooled in liquid nitrogen. Data were collected at the Swiss Light Source X06SA beamline on a Mar225 CCD detector. Initial crystals displayed approximately 8 Å maximum resolution, but several lines of crystal improvement, such as dehydration and detergent mixtures, improved diffraction properties. Optimized crystals diffracted anisotropically to at least 3.3 Å in the best direction, and about 4.5 Å in the worst direction. Heavy-atom derivatives were obtained by adding HoCl₃, K₂PtCl₆ or Ta₆Br₁₂ to the crystals before or during dehydration, either as salt or as a concentrated, aqueous solution.

Data processing. Data sets were processed using XDS³¹. The data quality was impaired by the strong anisotropy as also manifested by high R_{sym} values in the higher resolution bins (Supplementary Table 1). Initial heavy-atom positions were found using phases from a weak, low-resolution ($d > 8$ Å) molecular

replacement solution using PHASER³² and a partial search model derived from Ca²⁺-ATPase¹⁵. Phases from the HoCl₃ and K₂PtCl₆ data were obtained by multiple isomorphous replacement with anomalous scattering (MIRAS). Phases from the Ta₆Br₁₂ data were obtained by single isomorphous replacement with anomalous scattering (SIRAS). All phases were calculated by SHARP³³. Several native data sets were used to yield optimal isomorphous pairing of individual derivative data sets. The heavy-atom-derived phases were refined, combined and extended at the maximum resolution of the native data by density modification using dmmulti³⁴, exploiting two-fold rotational non-crystallographic symmetry, a solvent content of 75% and several data sets displaying low levels of isomorphism for inter-crystal averaging. The resulting electron-density map was of high quality, providing a continuous trace of the main chain, albeit with a limited level of detail owing to the anisotropy of the data (Fig. 2, and Supplementary Fig. 4). Refinement was focused on the fitting of a model with reasonable stereochemistry to the experimental map. Before refinement the data were anisotropically corrected using the Anisotropy Correction Server³⁵ (<http://www.doe-mbi.ucla.edu/~sawaya/anisocscale/>). The model was built using O (ref. 36) with a Ca²⁺-ATPase structure¹⁵ and the CopA N domain structure¹¹ as guides for chain tracing. Initial torsion-angle refinement, imposing strict non-crystallographic symmetry, was performed in CNS1.2 (ref. 37) using only higher resolution reflections (5–3.6 Å) without bulk solvent correction. Iterative model building and refinement gradually improved the model and the fit to the experimental map. In later stages, bulk solvent correction was applied using phenix.refine³⁸ along with tight non-crystallographic symmetry restraints and use of the reflections in the 20–3.6 Å range. The final model yielded a crystallographic *R*-factor of 35.0% and a free *R*-factor of 36.6%. PROCHECK³⁹ evaluation of the ramachandran plot gave 52.8% in core regions, 38.0% in allowed regions, 8.1% in generously allowed regions and 1.1% in disallowed regions. Cavities in the model were located using Voidoo⁴⁰. The full-length data were processed by XDS³¹ and a molecular replacement solution was obtained using PHASER³² and our model from the truncated form of AHA2. All figures were prepared using PyMOL⁴¹.

31. Kabsch, W. Automatic processing of rotation diffraction data from crystals of initially unknown symmetry and cell constants. *J. Appl. Cryst.* **26**, 795–800 (1993).
32. Storoni, L. C., McCoy, A. J. & Read, R. J. Likelihood-enhanced fast rotation functions. *Acta Crystallogr. D* **60**, 432–438 (2004).
33. de La Fortelle, E. & Bricogne, G. Maximum-likelihood heavy-atom parameter refinement for multiple isomorphous replacement and multiwavelength anomalous diffraction methods. *Macromol. Crystallogr. A* **276**, 472–494 (1997).
34. Cowtan, K. 'dm': An automated procedure for phase improvement by density modification. *CCP4 ESF-EACBM Newsletter Prot. Crystallogr.* **31**, 34–38 (1994).
35. Strong, M. *et al.* Toward the structural genomics of complexes: Crystal structure of a PE/PPE protein complex from *Mycobacterium tuberculosis*. *Proc. Natl Acad. Sci. USA* **103**, 8060–8065 (2006).
36. Jones, T. A., Zou, J. Y., Cowan, S. W. & Kjeldgaard, M. Improved methods for building protein models in electron-density maps and the location of errors in these models. *Acta Crystallogr. A* **47**, 110–119 (1991).
37. Brunger, A. T. *et al.* Crystallography & NMR system: A new software suite for macromolecular structure determination. *Acta Crystallogr. D Biol. Crystallogr.* **54**, 905–921 (1998).
38. Afonine, P. V., Grosse-Kunstleve, R. W. & Adams, P. D. A robust bulk-solvent correction and anisotropic scaling procedure. *Acta Crystallogr. D* **61**, 850–855 (2005).
39. Laskowski, R. A., MacArthur, M. W., Moss, D. S. & Thornton, J. M. Procheck—a program to check the stereochemical quality of protein structures. *J. Appl. Cryst.* **26**, 283–291 (1993).
40. Kleywegt, G. J. & Jones, T. A. Detection, delineation, measurement and display of cavities in macromolecular structures. *Acta Crystallogr. D* **50**, 178–185 (1994).
41. DeLano, W. L. The PyMOL molecular graphics system on the world wide web. (<http://www.pymol.org>) (2002).